Low-temperature and fast-charge sodium metal batteries

Low-Temperature and Fast-Charge Sodium Metal Batteries

Dandan Yu, Zhenya Wang, Jiacheng Yang, Yingyu Wang, Yuting Li, Qiaonan Zhu, Xinman Tu, Dezhi Chen, Junfei Liang, Umedjon Khalilov, and Hua Wang**

Dr. D. Yu, Prof. X. Tu, Prof. D. Chen

Key Laboratory of Jiangxi Province for Persistent Pollutants Control and Resources Recycle, School of Environmental and Chemical Engineering, Nanchang Hangkong University, Nanchang 330063, China

E-mail: chendz@nchu.edu.cn

Dr. D. Yu

College of Materials and Chemistry, China Jiliang University, Hangzhou 310018, China

Z. Wang, Y. Wang, J. Yang, Y. Li, Q. Zhu, Prof. H. Wang

School of Chemistry, Beijing Advanced Innovation Center for Biomedical Engineering, Beihang University, Beijing 100191, China

E-mail: wanghua8651@buaa.edu.cn

Prof. J. Liang

School of Energy and Power Engineering, North University of China, Taiyuan 030051, China

Dr. U. Khalilov

Department of Chemistry, University of Antwerp, Universiteitsplein 1, 2610, Antwerp, Belgium

Abstract: Low-temperature operation of sodium metal batteries (SMBs) at the high rate faces challenges of unstable solid electrolyte interphase (SEI), Na dendrite growth, and sluggish Na^+ transfer kinetics, causing a largely capacity curtailment. Herein, low-temperature and fast-charge SMBs were successfully constructed by synergetic design of the electrolyte and electrode. The optimized weak-solvation dual-salt electrolyte enables high Na plating/stripping reversibility and the formation of NaF-rich SEI layer to stabilize sodium metal. Moreover, an integrated copper sulfide electrode is *in-situ* fabricated by directly chemical sulfuration of copper current collector with micro-sized sulfur particles, which significantly improves the electronic conductivity and Na^+ diffusion, knocking down the kinetic barriers. Consequently, this SMB achieves the reversible capacity of 202.8 mAh g^{-1} at −20°C and 1 C (1 C=558 mA g^{-1}). Even at −40°C, a high capacity of 230.0 mAh g^{-1} can still be delivered at 0.2 C. This study is encouraging for further exploration of cryogenic alkali metal batteries, and enriches the electrode material for low-temperature energy storage.

Keywords: alkali metal anode, electrolyte, copper sulfide, low-temperature performance, sodium-ion batteries

1. Introduction

There is an growing demand for low-temperature batteries in real situations such as electric vehicles, submarine operations, space/polar exploration, and national defense.[1-3] The low-temperature operation usually leads to the high overpotentials and severe capacity loss, resulting from slow ion diffusion and difficult desolvation process associated with bulk electrolyte and electrode/electrolyte interphase, as well as the sluggish kinetics of electrode reactions.[4-7] And the battery polarization further increases at high current densities, which cause the inevitably metal plating at the anode side and even dendrite formation.[6,7] As an alternative to lithium (Li) metal, sodium (Na) metal is an attractive anode due to the naturally abundance, high theoretical capacity (1166 mAh g^{-1}), and low redox potential of Na/Na^+ (−2.71 V *vs.* standard hydrogen electrode).[8-10] Na has a lower first ionization energy than Li, which may benefit electrochemical reactions under cryogenic conditions.[9] More importantly, the weakly bound solvation shell of Na^+ indicates the low energy barrier for Na^+ desolvation as compared to the Li^+ counterpart.[11] Besides, Na^+-based electrolytes generally possess stronger ion-diffusion ability than the corresponding Li^+ electrolyte due to the weaker Lewis acidity and smaller Stokes radius of Na^+ than those of Li^+.[12] Thus, sodium metal batteries (SMBs) hold considerable promise for fast charging at subzero temperatures.

In cold climates, sodium metal anode still faces fundamental issues of low Coulombic efficiency (CE) for Na plating/striping, unstable solid electrolyte interphase (SEI), and dendrite growth.[13,14] Currently, electrolyte regulation and interphase engineering strategies have significantly improved the CE and cycle life of sodium metal anode at subzero temperatures and high current densities.[8,9,12-15] Electrode materials play significant roles in determining the low-temperature performance of SMBs. Typically, hard carbon exhibits low sodiation potential in the range of 0.01~0.10 V, leading to pernicious sodium plating at subzero temperatures.[16,17] Titanium-based

oxide materials such as $Na_2Ti_3O_7$, $NaV_{1.25}Ti_{0.75}O_4$, and $Ti_{0.88}Nb_{0.88}O_{4-x}$ have high working potentials for avoiding sodium deposition, whereas their low capacity cannot meet the increasing requirement for high energy.[18-20] Additionally, alloy- (Bi, Sn etc.), conversion- (such as Se) and intercalation/conversion-type (NbSSe, Co_3S_4@NiS_2 etc.) electrodes have been utilized for Na^+ storage under cryogenic conditions.[21-26] Although they can provide high-rate capacity and suitable potential plateau, the sophisticated nanostructural design is generally required to resist the volume variation during cycling. Therefore, it is urgently needed to explore new electrode materials for the advancement of low-temperature SMBs.

Herein, we successfully constructed a low-temperature and fast-charge SMB through simultaneous electrolyte engineering and electrode design. The weak solvation of 0.25 M sodium trifluoromethanesulfonate (NaOTF) and 0.25 M sodium hexafluorophosphate ($NaPF_6$) dissolved in diethylene glycol dimethyl ether (G2) with the 1,1,2,2-tetrafluoroethyl-2,2,3,3-tetrafluoropropylether (TTE) additive contributes to fast ion transportation for smooth Na plating behavior and the formation of NaF-rich solid-electrolyte interphase (SEI) layer. By simply coating micro-sized sulfur particles on the copper (Cu) current collector, copper sulfide (CuS) can be *in-situ* spontaneously fabricated as the electrode active material, which promotes the mass transport of charge carriers and reaction kinetics. These factors jointly endow the as-assembled SMB with a high capacity of 202.8 mAh g^{-1} at −20°C and 1 C (1 C=558 mA g^{-1}), spurring the development of SMBs for low-temperature applications.

2. Results and discussion

Impacts of electrolyte composition on the stability of Na metal anode

G2-based electrolytes including 1 M $NaPF_6$/G2, 1 M NaOTF/G2, 0.5 M $NaPF_6$-0.5 M NaOTF/G2 show good compatibility with Na metal at −20°C, where the dual-salt electrolyte enables the low overpotential of Na//Na symmetrical cells (Figure S1a) and high CE of Na//carbon-coated aluminum (Al@C) half cells at −20°C (Figure S1b, c), which might be attributed to the weak solvation for smooth Na plating/stripping.[8] To further improve the low-temperature adaptability of electrolyte, the concentration of

each salt was decreased to 0.25 M, and the TTE additive at the volume ratio of 3% was introduced to form stable interphase films as previous reported alkali metal batteries.[4,27,28] When being operated at −20°C, the Na//Al@C half-cell based on the 0.25 M $NaPF_6$-0.25 M NaOTF/G2/3%TTE electrolyte exhibits an average CE as high as 99.36% during 100 cycles at the current density of 0.5 mA cm^{-2} and the plating capacity of 0.5 mAh cm^{-2} (Figure 1a), whereas the gradually decrease in CEs upon cycling with large fluctuation happens as the dual-salt electrolyte without TTE is used, which confirms the significant role of TTE in stabilizing Na metal. Moreover, the optimized dual-salt electrolyte also realizes the ultrahigh average CE of 99.89% at 25°C. Besides, the overpotential of 0.115 V can be maintained after 100 cycles at −20°C (Figure 1b) as compared to that of 0.07 V at 25°C (Figure S2). According to the modified test protocol proposed by Zhang et al.,[29] the average CE of Na plating/stripping at –20°C is calculated to be 99.98% under the conditions of 0.5 mA cm^{-2} and 0.5 mAh cm^{-2} (Figure 1c), which exceeds that operated at room temperature (99.89%). Thus, highly reversible Na plating/stripping can be achieved over a wide temperature range from 25°C to –20°C by adopting the low-concentrated dual-salt electrolyte with the TTE additive.

The superiority of the modified dual-salt electrolyte at subzero temperatures was further confirmed by assembling Na//Na symmetrical cells at different operating temperatures. Stable potential curves can be observed at 0.5 mA cm^{-2} and 0.5 mAh cm^{-2} under both room- and low-temperature conditions, and the overpotential remains stably with the values of 0.016 and 0.022 V at −20°C and −40°C, respectively (Figure 1d). The Na//Na symmetrical cell containing the optimized dual-salt electrolyte exhibits stable potential profiles for 560 h at −40°C (Figure 1e). By contrast, a sharp increase in overpotential can be observed from the symmetrical cell without TTE, indicating unstable Na deposition/stripping.[1] As for the rate performance (Figure 1f), Na//Na symmetrical cells with the optimized dual-salt electrolyte remain stable cycling and still present small overpotential when the current density increases from 0.5 to 3.0 mA cm^{-2} at −20°C (0.0066 and 0.048 V at 0.5 and 3.0 mA cm^{-2}, respectively). Meanwhile, they

can withstand the high current density up to 5.0 mA cm^{-2} at 25°C (Figure S3 and S4), which prove that the TTE-modified dual-salt electrolyte not only shows good compatibility with Na metal, but also promotes the ion-transfer kinetics, especially at the ultralow temperature.

Subsequently, the morphology of Na metal in symmetrical cells after cycling at different temperatures was characterized by scanning electron microscope (SEM) images. A rough surface can be detected when utilizing the TTE-free dual-salt electrolyte at both −40°C (Figure 2a) and 25°C (Figure S5a) with the capacity of 0.5 mAh cm^{-2} at 0.5 mA cm^{-2}. In sharp contrast, the TTE-modified dual-salt electrolyte enables a flat Na metal surface at the same condition (Figure 2b and Figure S5b). Optical microscope images (Figure S6) further confirm that the optimized dual-salt electrolyte can effectively protect Na metal at subzero temperatures. It should be mentioned that the surface of Na metal after cycling at −40°C is flatter and more uniform than that operated at 25°C, which could be attributed to less side reactions at low temperatures.[30] The TTE-modified dual-salt electrolyte still provides a low impedance of Na//Na symmetrical cells even at the ultra-low temperature of –40 °C (Figure S7). Besides, the composition of SEI layers formed on Na metals in Na//Na symmetrical cells after cycling in different electrolytes was analyzed by FTIR spectra (Figure 2c). The C-F and P-F signals are significant enhanced after introducing the TTE additive in electrolyte, which indicates the involvement of TTE in forming F-contained SEI layer.[4] Thus, the TTE-modified dual-salt electrolyte enables highly reversible Na plating/stripping and stable cycling of Na metal at sub-zero temperatures.

Spectral analysis and theoretical calculation about the electrolyte solvation

To disclose the underlying reasons for excellent Na metal reversibility and uniform Na deposition under cryogenic conditions, electrolyte solvation structures were investigated by FTIR spectra because the solvation environment of Na^+ in electrolyte generally defines the charge-transfer barrier. Compared with single G2 solvent, the introduction of $NaPF_6$ results in a large red-shift of the C–C–O bend/twist from 852 to 836.4 cm^{-1} due to the strong interaction between Na^+ and G2 (Figure 2d).[31]

Importantly, the blue shift happens when the NaOTF salt is further dissolved to prepare 1 M NaOTF-1 M $NaPF_6$/G2 (labeled as 1-1), suggesting the weakened binding strength in this dual-salt electrolyte.[32] When the concentration of each sodium salt decreases from 1 to 0.25 M, the 0.25 M NaOTF-0.25 M $NaPF_6$/G2 (labeled as 0.25-0.25) exhibits the signal around 842.8 cm^{-1}, owing to the weak solvation of low-concentrated electrolyte. It is worth noting that the TTE additive has little effect on the solvation structure except for the enhancement in C-F signals (Figure S8), which indicates that TTE does not participate in the electrolyte solvation.[33] Therefore, the TTE-modified dual-salt electrolyte enables a facile Na^+ desolvation at low temperatures.

Density functional theory (DFT) calculations were subsequently performed to gain deep understanding of solvation structures in the optimized dual-salt electrolyte. Apparently, the desolvation energy of Na^+–OTF^-–G2 complex (1.827 eV) is lower than that of Na^+–PF_6^-–G_2 (1.921 eV), which demonstrates that the Na^+–OTF^-–G_2 complex interaction is much weaker (Figure 2e).[34] It can be speculated that the introduction of NaOTF in $NaPF_6$/G2 electrolyte could effectively decrease the barrier for interfacial Na^+ transfer. Another significant impact for stabilizing Na metal is the composition of SEI layer. The lowest unoccupied molecular orbital (LUMO) energy levels of different ion-solvent complexes are considered to predict their reductive decomposition ability on the Na metal anode/electrolyte interface.[35] Importantly, the LUMO energy of Na^+–PF_6^-–G_2 complex (–0.030 eV) is lower than that of Na^+–OTF^-–G2 (0.121 eV), which demonstrates the decomposition of Na^+–PF_6^-–G_2 is preferred at the sodium metal anode side (Figure 2f). This result agrees well with the enhancement in C-F and P-F signals of SEI layer formed in the TTE-modified dual-salt electrolyte.

Electrochemical performance of sodium metal batteries

Considering the intrinsic high theoretical capacity for Na^+ storage, micro-sized sulfur particles were directly used as the active material in electrode to construct SMBs (Figure S9). SEM images show the apparent morphology change when micro-sized sulfur particles are coated on the Cu current collector (Figure S10). Abundant nanoparticles and porous structures can be *in-situ* constructed in electrode, which

facilitate the electrolyte penetration, especially for high-loading electrode. Moreover, X-ray diffraction (XRD) patterns (Figure S11a) indicate the transformation of partial sulfur (PDF#08-0247) into CuS (PDF#06-0464) and Cu_7S_4 (PDF#23-0958) when utilizing the Cu foil in electrode rather than aluminum (Al) foil. The *in-situ* chemical fabrication of CuS in Cu-S electrode (Figure S11b) can also be realized by casting the mixture of Cu powder (Figure S12) and micro-sized sulfur particles at the molar ratio of 1:1 on the Cu foil surface. Besides, XRD pattern of the electrode harvested from SMBs after standing period shows the diffraction peaks of CuS (Figure S13). This phenomenon is consistent with the reported cuprous selenide electrode, which can be prepared by directly chemical selenization of Cu current collector, for potassium-ion and sodium-ion storage.[34] CuS should be regarded as the electrochemical active composition in fresh electrode once the spontaneous conversion process happens completely. Importantly, CuS possesses high electronic conductivity (~10^{-3} S m^{-1}) and large interlayer spacing (~8.2 Å), which facilitate the electron transfer and Na^+ diffusion, especially at low temperatures.[36,37] Thus, the specific capacity of SMBs was calculated based on the theoretical mass of *in-situ* self-constructed CuS (1 C=558 mA g^{-1}), rather than sulfur in electrode.

Based on the TTE-modified dual-salt electrolyte, the as-assembled SMBs exhibit the high capacity of 283.4 mAh g^{-1} after 300 cycles at 2 C with an ultrahigh retention of 98.6% when being operated at 25℃ (Figure 3a). Notably, the variation in voltage plateaus during the initial activation process results from the composition change of electrode (Figure S14). Moreover, the capacities of 342.5, 318.6, 303.4, 289.1, 279.5, and 267.5 mAh g^{-1} can be attained at 0.2, 0.5, 1, 2, 3, and 5 C (Figure 3b), respectively. When the current density is set back to 0.2 C, the capacity recovers to 342.8 mAh g^{-1}, suggesting the excellent rate capability and highly reversibility of SMBs at room temperature. The multi-step electrochemical reaction process can be speculated from the charge-discharge profiles at different rates (Figure 3c), and meanwhile, small cathodic/anodic peak shift around 0.14 V when the scan rate increases from 0.4 to 2.0 mV s^{-1} further confirms the outstanding rate performance of SMBs (Figure 3d). When

the mass loading of sulfur in electrode increases to 6.8 mg cm^{-2}, SMBs still remain stable cycling performance with a high capacity of 288.8 mAh g^{-1} after 90 cycles at 0.1 C (Figure S15).

The low-temperature operation inevitably decreases the electrochemical reaction rate of electrode.[38-40] It should be mentioned that the optimized dual-salt electrolyte guarantees higher capacity of SMBs and more efficient utilization of electrode active material under cryogenic conditions compared with mono-salt electrolytes (Figure S16), suggesting good temperature adaptability of SMBs after the initial activation process at 25℃. At –20℃, SMBs containing the TTE-modified dual-salt electrolyte deliver the high capacity of 282.3 mAh g^{-1} after 40 cycles at 0.5 C (Figure 3e). When the temperature decreases to –40℃, the reversible capacity can reach up to 230.0 mAh g^{-1} after the initial 6 cycles at 0.2 C accompanying with the gradual recovery of discharge voltage plateaus, which is corresponded to 67.1% of the room-temperature capacity, and it can still be maintained at 218.2 mAh g^{-1} after 40 cycles. Moreover, the charge-discharge curves at sub-zero temperatures show the absence of third discharge voltage platform within 40 cycles (Figure 3f, g) in comparison to that at 25℃, which further confirms the limited reaction kinetics under cryogenic conditions.[39] Typically, SMBs deliver the capacities of 320.5, 291.7, and 202.8 mAh g^{-1} at different rates of 0.2, 0.5, and 1 C, respectively, when being operated at –20℃ (Figure 3h, i). And the capacity can be retained at 316.2 mAh g^{-1} as the current density returns to 0.2 C, demonstrating the excellent rate performance of SMBs at sub-zero temperatures. Notably, the overall low-temperature performance of our SMB is superior to those of reported SMBs (Figure S17).[16-21,24-26] Based on the Cu-S electrode fabricated by mixing Cu powder with micro-sized sulfur particles (Figure S18), SMBs also exhibit superior rate capability and cycling stability at both the room temperature (Figure S19) and sub-zero temperatures (Figure S20). Thus, the well-designed SMBs exhibit outstanding low-temperature adaptability, and the proposed synergetic strategy can be extended to other copper chalcogenide-based electrode materials.

Reaction mechanism of electrode and electrode/electrolyte interphase

The important role of Cu current collector in electrode can be confirmed by the low capacity at 25℃ and fast degradation at –40℃ when the Al foil is utilized to replace Cu (Figure S21). Unlike the Al foil, the utilization of Cu current collector in electrode results in low resistance of SMBs at both 25°C and –40°C (Figure S22). The SEM and elemental mapping images of fresh electrode show the uniform distribution of Cu, S, C and O elements on the electrode surface (Figure 4a and Figure S23). *Ex-situ* X-ray photoelectron spectroscopy (XPS) analysis was firstly carried out to clarify the variation in surface chemical compositions of fresh electrode and the electrodes harvested from SMBs at the cut-off voltages of 0.2 and 2.8 V after cycling at 0.2 C. In the XPS spectrum of fresh electrode, two peaks at 163.6 and 164.8 eV are derived from S $2p_{3/2}$ and S $2p_{1/2}$ of elemental S^0, while two peaks at 162.1 and 162.9 eV are assigned to the Cu-S bond (Figure 4b).[36,37,41,42] After being discharged to 0.2 V, the appearance of peak at 161.8 eV confirms the formation of Na_2S.[43,44] Moreover, two peaks at 162.8 and 164.0 eV are ascribed to Na_2S_4.[38,41] The Cu LMM Auger peak at 921 eV (Figure S24) confirms the presence of Cu^0.[45,46] When the electrode is recharged to 2.8 V, the peaks of Na_2S and Na_2S_4 disappear, while the Cu-S bonding is clearly discovered. Besides, the wide peak at 168.8 eV corresponding to sulfate stems from the oxidation of initial electrode or electrolyte decomposition.[44]

Subsequently, to further reveal the reaction mechanism of electrode in SMBs, *in-situ* XRD measurement was performed on SMBs during six cycles at 0.2 C and 25℃ (Figure 4c, d). Notably, there is no diffraction peak of sulfur at the beginning of first cycle (Figure 4e). Three peaks at 33.5°, 35.9° and 37.2° appear, which are assigned to the (0111), (1013) and (0114) planes of Cu_9S_5 (PDF#26-0476). Simultaneously, two diffraction peaks at 28.4° and 29.5° correspond to the (111) and (200) planes of $NaCu_5S_3$ (PDF#78-0613), and meanwhile, the peak at 32.7° belongs to the CuS (006) plane. Thus, the *in-situ* phase evolution of electrode during the standing period can be described as:

$$9S + 15Cu + Na^+ + e^- \rightarrow NaCu_5S_3 + Cu_9S_5 + CuS \quad (1)$$

At the discharge voltage of 0.9 V, the peak at 34.5° emerges, which is indexed to the (321) plane of Na_2S_4 (PDF#71-0516). As the discharge proceeds, the intensities of these peaks decrease significantly. When being discharged to 0.4 V, the peak at 23.5° appears, corresponding to the (111) plane of Na_2S (PDF#47-1698), and thus Na_2S is the final sodiation product. During the subsequent charge process, the peaks of Na_2S_4 and $NaCu_5S_3$ reappear sequentially at the voltages of 1.70 and 1.75 V. Moreover, the characteristic peak of Na_2S becomes weak and even vanishes until being charged to 1.8 V. The reappearance of Cu_9S_5 and CuS happens at charge voltages of 1.8 and 2.2 V, respectively. In the second cycle, the enhanced peaks located at 28.4°, 29.5°, 35.7° and 38.7° can be observed at the discharge voltage of 1.2 V, which are assigned to the (111), (200), (112) and (202) planes of $NaCu_5S_3$, respectively.[45] Based on the experimental results and reported studies,[4,46,47] the reversible phase evolution during cycling can be expressed as follows:

$$2NaCu_5S_3 + 10Na^+ + 10e^- \leftrightarrow 6Na_2S + 10Cu \quad (2)$$

$$Cu_9S_5 + 10Na^+ + 10e^- \leftrightarrow 5Na_2S + 9Cu \quad (3)$$

$$CuS + 2Na^+ + 2e^- \leftrightarrow Na_2S + Cu \quad (4)$$

More importantly, XRD patterns of electrodes during fourth and fifth cycles at the cut-off voltages further confirm the conversion reaction between $NaCu_5S_3$/CuS/Cu_9S_5 and Na_2S (Figure 4f).

In addition, the adsorption energy of Na_2S_4 on CuS (−4.19 eV) is much lower than that of S (−2.21 eV) (Figure 5a), indicating that CuS presents stronger adsorption capability towards Na_2S_4 as a typical soluble polysulfide intermediate, and thus the polysulfide dissolution in SMBs can be significantly mitigated.[48] To investigate the compositions of electrode/electrolyte interphase layers formed in the TTE-modified dual-salt electrolyte, *semi-in situ* XPS characterization of the electrode and Na metal anode in SMBs was conducted at different etching time after three cycles at 0.2 C and 25°C. Regarding the CuS-based electrode, the low atomic ratio of P (Figure S25) suggests the less oxidative decomposition of PF_6^- anions compared with OTF^-. According to the difference in the calculated highest occupied molecular orbital

(HOMO) energy level, F-contained compounds might be primary from the Na^+–OTF^-–G2 complex (–7.46 eV *vs.* –7.59 eV for Na^+–PF_6^-–G2, Figure 2f). Moreover, F 1s spectra (Figure 5b) and C 1s spectra (Figure S26a) confirm the formation of organic-inorganic interphase layer on the integrated CuS electrode.[49,50] A NaF-rich SEI layer (Figure 5c and Figure S26b) can be formed on the Na metal surface. Remarkably, the NaF content increases significantly with the etching time (Figure 5d), which endows the SEI layer with good mechanical strength to suppress Na dendrite growth. Thus, the *in-situ* self-constructed CuS (Figure 5e) in electrode before cycling can improve the electrode reaction kinetics and restrain the polysulfide detachment. Moreover, the weak solvation effect of the TTE-modified dual-salt electrolyte is capable of building NaF-rich SEI layer to stabilize Na metal anode, resulting in the excellent low-temperature performance of SMBs.

3. Conclusion

In summary, we have successfully built a low-temperature and fast-charge SMB by combining a weakly solvated electrolyte with a facile electrode design. The TTE-modified dual-salt electrolyte enables high reversibility of Na plating/stripping, the formation of NaF-rich SEI layer, and dendrite-free Na metal anode at sub-zero temperatures. Moreover, the *in-situ* fabrication of CuS in electrode not only plays significant role in boosting the electrode conductivity and reaction kinetics, but also greatly enhances the anchoring strength towards Na_2S_4 as the intermediate product, allowing for reversible and fast conversion process. As a result, the well-designed SMB shows high capacity and good low-temperature adaptability. When being operated at –20°C, our SMB delivers a high capacity of 202.8 mAh g^{-1} at 1 C. Even at the ultralow temperature of –40°C, the reversible capacity is still as high as 230.0 mAh g^{-1} at 0.2 C. This synergetic design strategy provides new insights for future development of low-temperature alkali metal batteries.

Acknowledgements

The authors acknowledge the financial support of the National Natural Science Foundation of China (52002081, 21972007 and 52172178), International Cooperation Project of National Key Research and Development Program of China (2022YFE0126300), and the Natural Science Foundation of Beijing (2222059). This research was supported by the high performance computing (HPC) resource at Beihang University.

Conflict of Interest

The authors declare no conflict of interest.

References

[1] X. Zheng, Z. Gu, J. Fu, H. Wang, X. Ye, L. Huang, X. Liu, X. Wu, W. Luo, Y. Huang, *Energy Environ. Sci.* **2021**, *14*, 4936-4947.
[2] X.-X. Gu, S. Qiao, X.-L. Ren, X.-Y. Liu, Y.-Z. He, X.-T. Liu, T.-F. Liu, *Rare Met.* **2021**, *40*, 828-836.
[3] Y. Yang, W. Yang, H. Yang, H. Zhou, *eScience* **2023**, *3*, 100170.
[4] J. Chen, D. Yu, Q. Zhu, X. Liu, J. Wang, W. Chen, R. Ji, K. Qiu, L. Guo, H. Wang, *Adv. Mater.* **2022**, *34*, 2205678.
[5] R. Xu, S. Zhang, X. Shen, N. Yao, J.-F. Ding, Y. Xiao, L. Xu, C. Yan, J.-Q. Huang, *Small Struct.* **2023**, *4*, 202200400.
[6] X. Wang, L. Yang, N. Ahmad, L. Ran, R. Shao, W. Yang, *Adv. Mater.* **2023**, *35*, 2209140.
[7] J. Xu, J. Zhang, T. P. Pollard, Q. Li, S. Tan, S. Hou, H. Wan, F. Chen, H. He, E. Hu, K. Xu, X.-Q. Yang, O. Borodin, C. Wang, *Nature* **2023**, *614*, 694-700.
[8] J. Zhou, Y. Wang, J. Wang, Y. Liu, Y. Li, L. Cheng, Y. Ding, S. Dong, Q. Zhu, M. Tang, Y. Wang, Y. Bi, R. Sun, Z. Wang, H. Wang, *Energy Storage Mater.* **2022**, *50*, 47-54.
[9] C. Wang, A. C. Thenuwara, J. Luo, P. P. Shetty, M. T. McDowell, H. Zhu, S. Posada-Pérez, H. Xiong, G. Hautier, W. Li, *Nat. Commun.* **2022**, *13*, 4934.
[10] H. Wang, D. Yu, C. Kuang, L. Cheng, W. Li, X. Feng, Z. Zhang, X. Zhang, Y. Zhang, *Chem* **2019**, *5*, 1-26.
[11] T. P. Liyana-Arachchi, J. B. Haskins, C. M. Burke, K. M. Diederichsen, B. D. McCloskey, J. W. Lawson, *J. Phys. Chem. B* **2018**, *122*, 8548-8559.
[12] S. Zhong, Y. Yu, Y. Yang, Y. Yao, L. Wang, S. He, Y. Yang, L. Liu, W. Sun, Y. Feng, H. Pan, X. Rui, Y. Yu, *Angew. Chem. Int. Ed*. **2023**, *62*, e202301169.
[13] A. C. Thenuwara, P. P. Shetty, N. Kondekar, C. Wang, W. Li, M. T. McDowell, *J.*

Mater. Chem. A **2021**, *9*, 10992-11000.
[14] X. Hu, E. Matios, Y. Zhang, C. Wang, J. Luo, W. Li, *Angew. Chem. Int. Ed.* **2021**, *60*, 5978-5983.
[15] X. Xia, S. Xu, F. Tang, Y. Yao, L. Wang, L. Liu, S. He, Y. Yang, W. Sun, C. Xu, Y. Feng, H. Pan, X. Rui, Y. Yu, *Adv. Mater.* **2023**, *35*, 2209511.
[16] X. Yin, Z. Lu, J. Wang, X. Feng, S. Roy, X. Liu, Y. Yang, Y. Zhao, J. Zhang, *Adv. Mater.* **2022**, *34*, 2109282.
[17] C. Yang, X. Liu, Y. Lin, L. Yin, J. Lu, Y. You, *Adv. Mater.* **2023**, *35*, 2301817.
[18] W. Meng, Z. Dang, D. Li, L. Jiang, *Adv. Mater.* **2023**, *35*, 2301376.
[19] Q. Li, K. Jiang, X. Li, Y. Qiao, X. Zhang, P. He, S. Guo, H. Zhou, *Adv. Energy Mater.* **2018**, *8*, 1801162.
[20] H. Liang, L. Liu, N. Wang, W. Zhang, C.-T. Hung, X. Zhang, Z. Zhang, L. Duan, D. Chao, F. Wang, Y. Xia, W. Li, D. Zhao, *Adv. Mater.* **2022**, *34*, 2202873.
[21] Z. Li, Y. Zhang, J. Zhang, Y. Cao, J. Chen, H. Liu, Y. Wang, *Angew. Chem. Int. Ed.* **2022**, *61*, e202116930.
[22] C. Wang, D. Du, M. Song, Y. Wang, F. Li, *Adv. Energy Mater.* **2019**, *9*, 1900022.
[23] J. Yang, X. Guo, H. Gao, T. Wang, Z. Liu, Q. Yang, H. Yao, J. Li, C. Wang, G. Wang, *Adv. Energy Mater.* **2023**, *13*, 2300351.
[24] Y.-Y. Wang, B.-H. Hou, J.-Z. Guo, Q.-L. Ning, W.-L. Pang, J. Wang, C.-L. Lü, X.-L. Wu, *Adv. Energy Mater.* **2018**, *8*, 1703252.
[25] L.-F. Zhou, X.-W. Gao, T. Du, H. Gong, L.-Y. Liu, W.-B. Luo, *Chem. Eng. J.* **2022**, *435*, 134838.
[26] X. Huang, R. Wang, L. Wu, H. Zhang, J. Liu, *Small* **2023**, *19*, 2304165.
[27] K. Park, Y. Jo, B. Koo, H. Lee, H. Lee, *Chem. Eng. J.* **2022**, *427*, 131889.
[28] X. Ren, X. Zhang, Z. Shadike, L. Zou, H. Jia, X. Cao, M. H. Engelhard, B. E. Matthews, C. Wang, B. W. Arey, X.-Q. Yang, J. Liu, J.-G. Zhang, W. Xu, *Adv. Mater.* **2020**, *32*, 2004898.
[29] B. D. Adams, J. Zheng, X. Ren, W. Xu, J.-G. Zhang, *Adv. Energy Mater.* **2018**, *8*, 1702097.
[30] X. Liu, X. Zheng, X. Qin, Y. Deng, Y. Dai, T. Zhao, Z. Wang, H. Yang, W. Luo, *Nano Energy* **2022**, *103*, 107746.
[31] J. Yang, J. Ruan, Q. Li, F. Fang, Y. Song, D. Sun, F. Wang, *Adv. Funct. Mater.* **2022**, *32*, 2200566.
[32] Z. Lu, H. Yang, Q.-H. Yang, P. He, H. Zhou, *Angew. Chem. Int. Ed.* **2022**, *61*, e202200410.
[33] B. Nan, L. Chen, N. D. Rodrigo, O. Borodin, N. Piao, J. Xia, T. Pollard, S. Hou, J. Zhang, X. Ji, J. Xu, X. Zhang, L. Ma, X. He, S. Liu, H. Wan, E. Hu, W. Zhang, K. Xu, X.-Q. Yang, B. Lucht, C. Wang, *Angew. Chem. Int. Ed.* **2022**, *61*, e202205967.
[34] X. Chen, M. Li, S.-P. Wang, C. Wang, Z. Shen, F.-Q. Bai, F. Du, *Adv. Sci.* **2022**, *9*, 2104630.
[35] W. Luo, D. Yu, J. Yang, H. Chen, J. Liang, L. Qin, Y. Huang, D. Chen, *Chem. Eng. J.* **2023**, *473*, 145312.
[36] Y. Wang, D. Chao, Z. Wang, J. Ni, L. Li, *ACS Nano* **2021**, *15*, 5420-5427.
[37] J. Zhang, Q. Lei, Z. Ren, X. Zhu, J. Li, Z. Li, S. Liu, Y. Ding, Z. Jiang, J. Li, Y.

Huang, X. Li, X. Zhou, Y. Wang, D. Zhu, M. Zeng, L. Fu, *ACS Nano* **2021**, *15*, 17748-17756.
[38] C.-Y. Fan, Y.-P. Zheng, X.-H. Zhang, Y.-H. Shi, S.-Y. Liu, H.-C. Wang, X.-L. Wu, H.-Z. Sun, J.-P. Zhang, *Adv. Energy Mater.* **2018**, *8*, 1703638.
[39] F. Chu, M. Wang, J. Liu, Z. Guan, H. Yu, B. Liu, F. Wu, *Adv. Funct. Mater.* **2022**, *32*, 2205393.
[40] D. Yu, K. Li, G. Ma, F. Ru, X. Zhang, W. Luo, P. Hu, D. Chen, H. Wang, *ChemSusChem* **2023**, *16*, 202201595.
[41] M. Geng, H. Yang, C. Shang, *Adv. Sci.* **2022**, *9*, 2204561.
[42] X. Ye, J. Ruan, Y. Pang, J. Yang, Y. Liu, Y. Huang, S. Zheng, *ACS Nano* **2021**, *15*, 5639-5648.
[43] S. Zhang, Y. Yao, X. Jiao, M. Ma, H. Huang, X. Zhou, L. Wang, J. Bai, Y. Yu, *Adv. Mater.* **2021**, *33*, 2103846.
[44] Y. Jiang, Z. Yu, X. Zhou, X. Cheng, H. Huang, F. Liu, Y. Yang, S. He, H. Pan, H. Yang, Y. Yao, X. Rui, Y. Yu, *Adv. Mater.* **2023**, *35*, 2208873.
[45] Y. Xiao, D. Su, X. Wang, S. Wu, L. Zhou, Y. Shi, S. Fang, H.-M. Cheng, F. Li, *Adv. Energy Mater.* **2018**, *8*, 1800930.
[46] C. Lu, A. Li, G. Li, Y. Yan, M. Zhang, Q. Yang, W. Zhou, L. Guo, *Adv. Mater.* **2021**, *33*, 2008414.
[47] C. Dai, L. Hu, X. Jin, H. Chen, X. Zhang, S. Zhang, L. Song, H. Ma, M. Xu, Y. Zhao, Z. Zhang, H. Cheng, L. Qu, *Adv. Mater.* **2021**, *33*, 2105480.
[48] Z. Yan, J. Xiao, W. Lai, L. Wang, F. Gebert, Y. Wang, Q. Gu, H. Liu, S.-L. Chou, H. Liu, S.-X. Dou, *Nat. Commun.* **2019**, *10*, 4793.
[49] P. M. L. Le, T. D. Vo, H. Pan, Y. Jin, Y. He, X. Cao, H. V. Nguyen, M. H. Engelhard, C. Wang, J. Xiao, J.-G. Zhang, *Adv. Funct. Mater.* **2020**, *30*, 2001151.
[50] D. Yu, Q. Zhu, L. Cheng, S. Dong, X. Zhang, H. Wang, N. Yang, *ACS Energy Lett.* **2021**, *6*, 949-958.

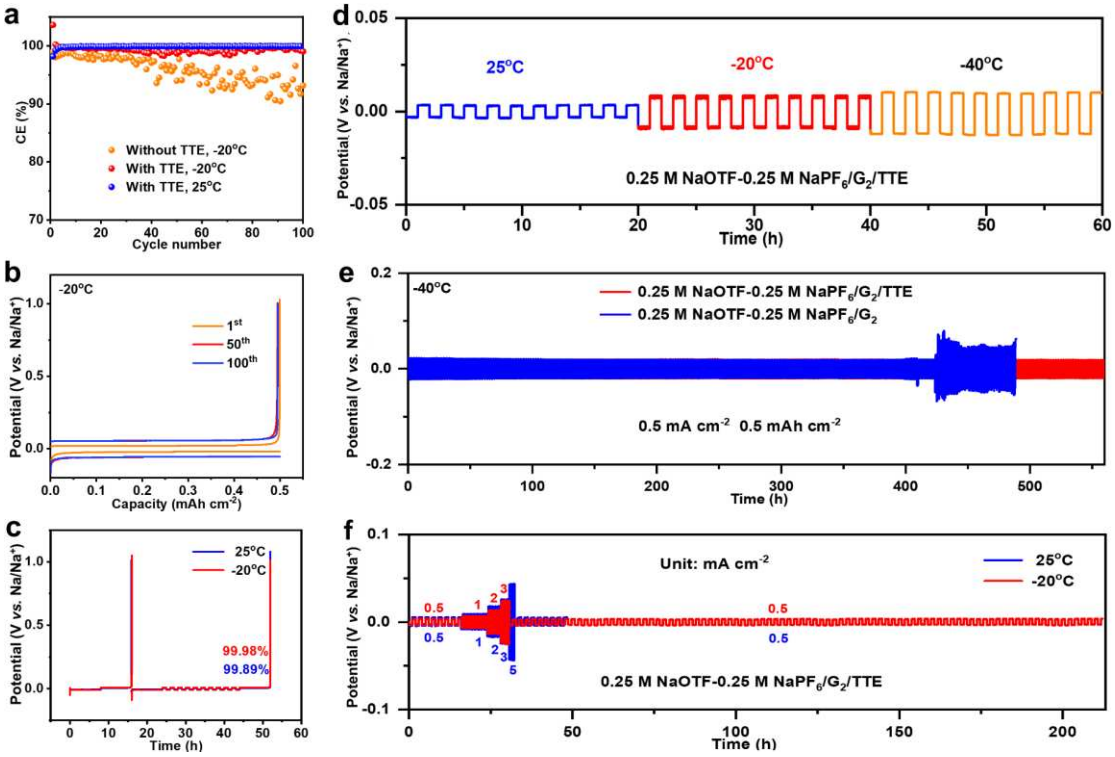

Figure 1. (a) Coulombic efficiencies of Na//Al@C half cells using 0.25 M $NaPF_6$-0.25 M NaOTF/G2/3%TTE and 0.25 M $NaPF_6$-0.25 M NaOTF/G2 electrolytes at different temperatures with the plating capacity of 0.5 mAh cm^{-2} at the current density of 0.5 mA cm^{-2} under the charge cut-off potential of 1.0 V, and (b) the representative potential capacity curves of Na//Al@C half cells based on the TTE-modified dual-salt electrolyte at –20°C. (c) Average CE measurements of Na//Al@C half cells at 0.5 mA cm^{-2} and 0.5 mAh cm^{-2} using modified test protocol proposed by Zhang and co-workers. (d) Galvanostatic profiles of Na//Na symmetrical cells using the TTE-modified dual-salt electrolyte from 25°C to –40°C at the current density of 0.5 mA cm^{-2} and the capacity of 0.5 mAh cm^{-2}. (e) Galvanostatic profiles of Na//Na symmetrical cells using 0.25 M $NaPF_6$-0.25 M NaOTF/G2/3%TTE and 0.25 M $NaPF_6$-0.25 M NaOTF/G2 electrolytes at –40°C with the capacity of 0.5 mAh cm^{-2} at the current density of 0.5 mA cm^{-2}. (f) Galvanostatic profiles of Na//Na symmetrical cells using the 0.25 M $NaPF_6$-0.25 M NaOTF/G2/3%TTE electrolyte at 25°C and –40°C with the capacity of 0.5 mAh cm^{-2} at different current densities.

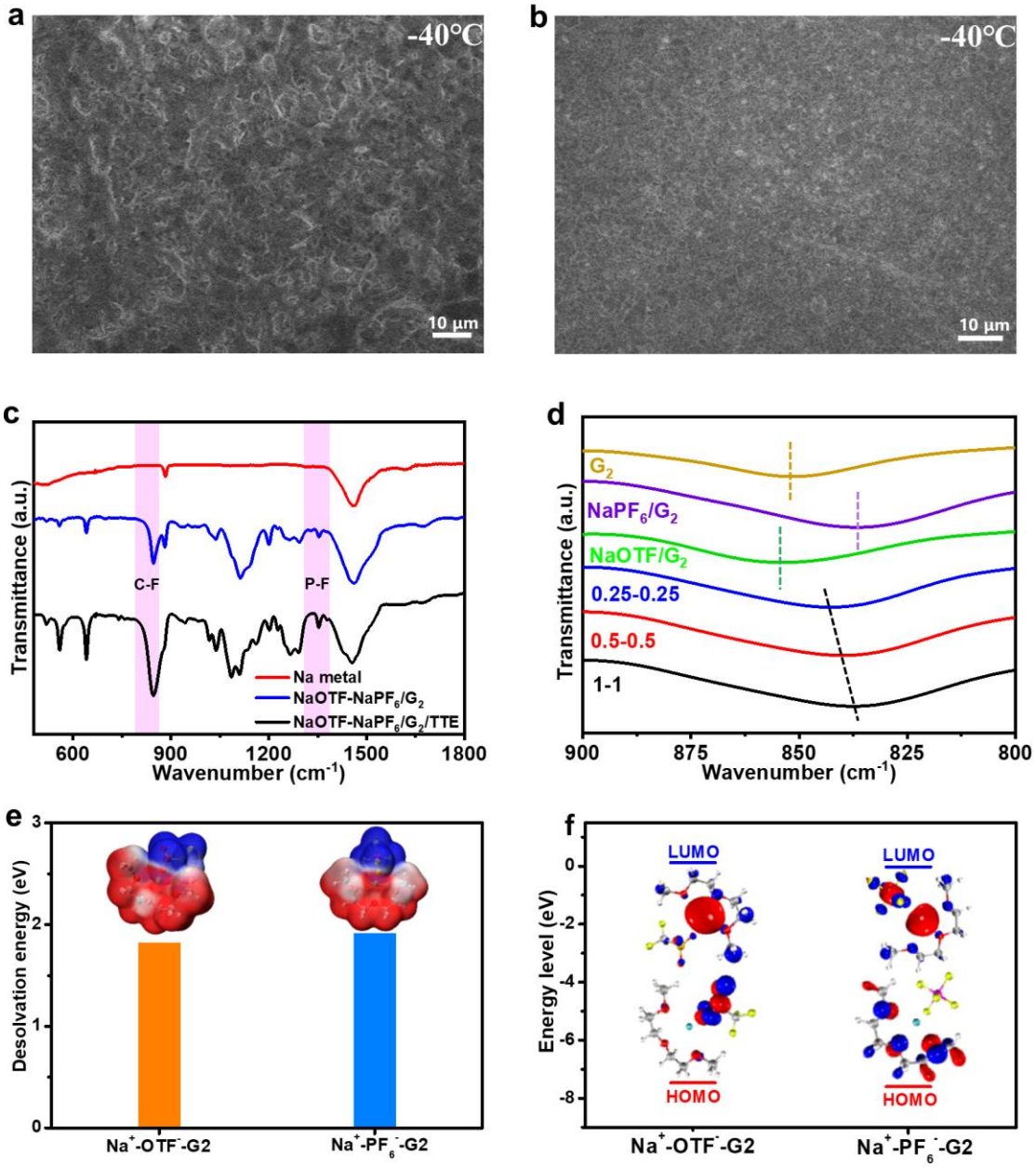

Figure 2. SEM images of Na metals disassembled from Na//Na symmetrical cells using (a) 0.25 M $NaPF_6$-0.25 M NaOTF/G2 and (b) 0.25 M $NaPF_6$-0.25 M NaOTF/G2/3%TTE electrolytes after 10 cycles at –40°C. (c) FTIR spectra of fresh Na metal and Na metals disassembled from Na//Na symmetrical cells using two dual-salt electrolytes with and without the TTE additive after 10 cycles at –40°C. (d) FTIR spectra of G2, 1 M NaOTF/G2, 1 M NaOTF/G2 and dual-salt electrolytes with different salt concentration of 0.25, 0.5, and 1 M. (e) Desolvation energy of Na^+–OTF^-–G2 and Na^+–PF_6^-–G2 complexes. (f) HOMO-LUMO energy levels of Na^+–OTF^-–G2 and Na^+–PF_6^-–G2. Green, pink, yellow, orange, red, grey, and light gray balls represent Na, P, F, S, O, C and H atoms, respectively.

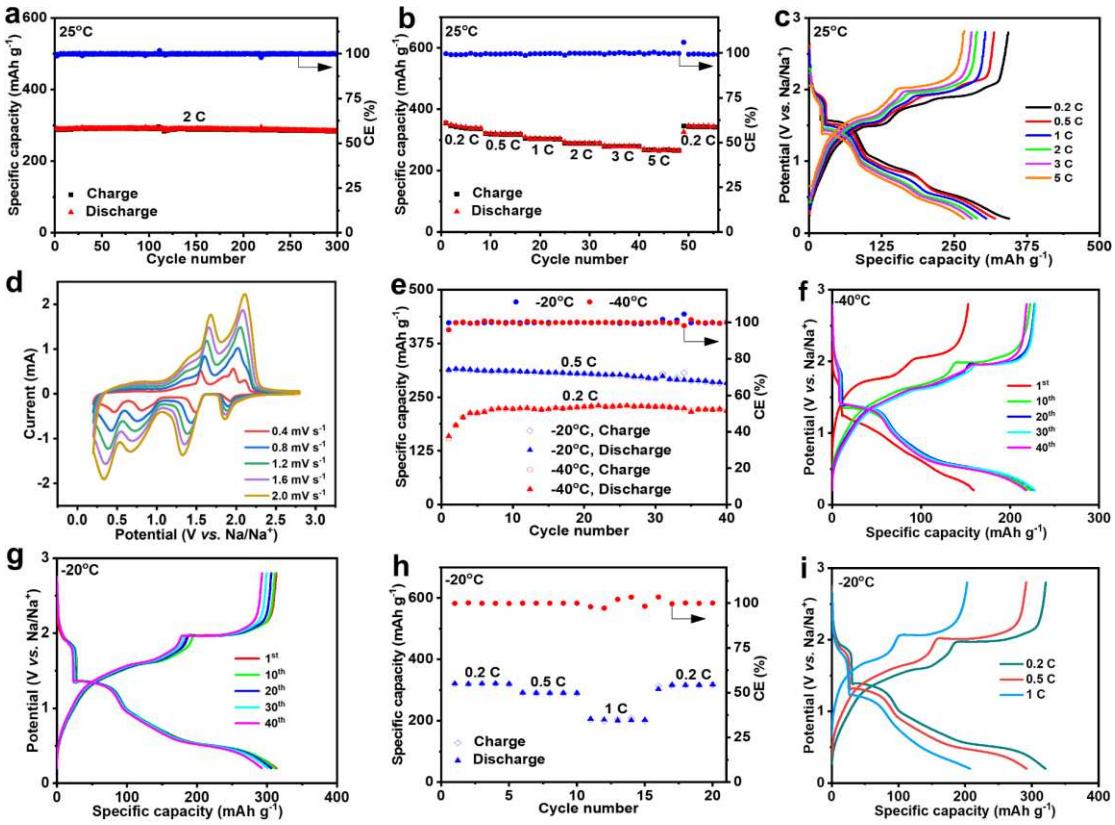

Figure 3. Electrochemical performance of sodium metal batteries using the 0.25 M $NaPF_6$-0.25 M NaOTF/G2/3%TTE electrolyte and micro-sized sulfur particles coated on the Cu collector as electrode. Room-temperature (a) cycling performance at 2 C, (b) rate capability, and (c) the corresponding charge-discharge profiles at different rates. (d) CV curves at 25°C. (e) Cycling performance at –20°C and –40°C with the current densities of 0.5 C and 0.2 C, respectively. The representative charge-discharge profiles at (f) –40°C and (g) –20°C with the current densities of 0.2 C and 0.5 C, respectively. (h) Rate capability at –20°C and (i) the corresponding charge-discharge profiles at different rates.

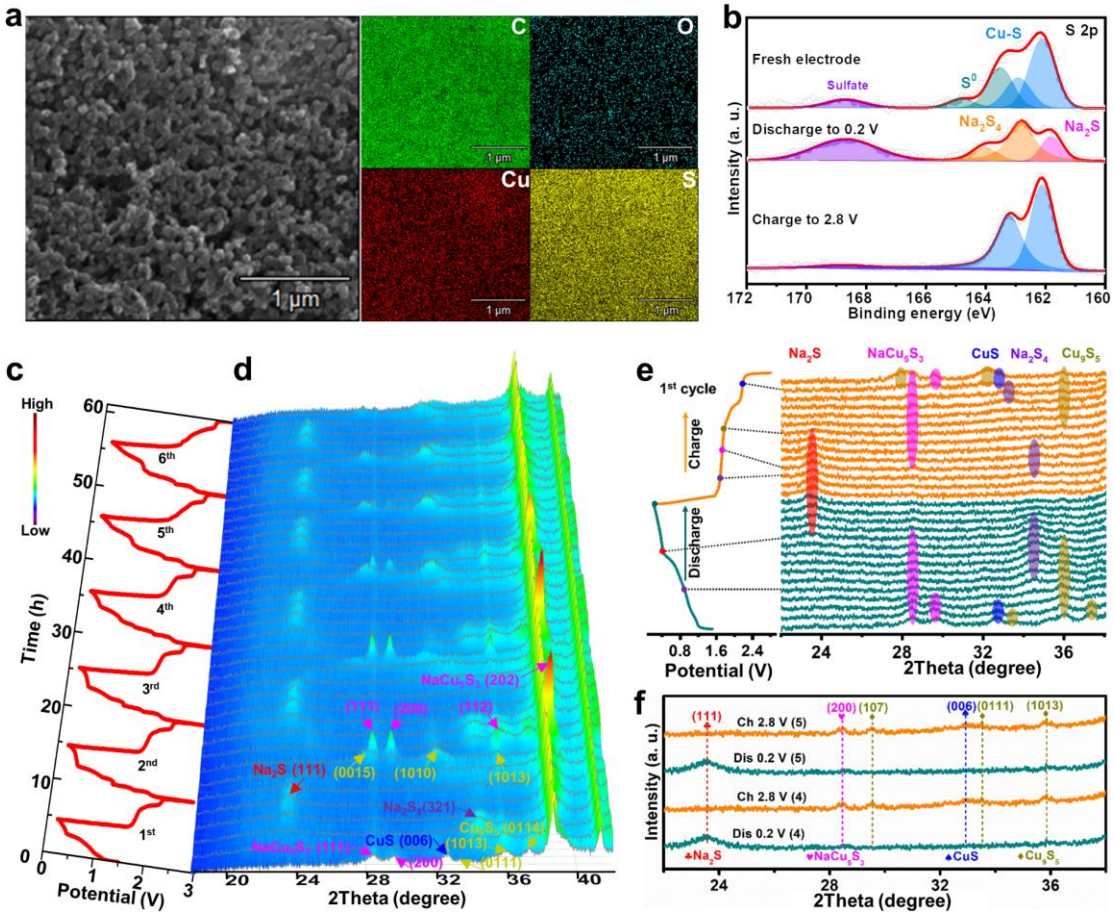

Figure 4. (a) The SEM image and the corresponding elemental mapping images of fresh electrode prepared by coating micro-sized sulfur particles on the Cu current collector. (b) The S 2p spectra of fresh electrode and the electrodes harvested from sodium metal batteries when being discharged to 0.2 V and recharged to 2.8 V, respectively, after cycling at 0.2 C and 25°C. (c) The charge-discharge profiles of sodium metal batteries during the initial six cycles at 0.2 C, and (d) the corresponding *in-situ* XRD patterns of electrode. (e) *In-situ* XRD patterns of the electrode at different states during the first cycle at 0.2 C. (f) *In-situ* XRD patterns of the electrode at the cut-off voltages during the fourth (labeled as (4)) and fifth (labeled as (5)) cycles at 0.2 C, where Dis and Ch represent discharge and charge states, respectively.

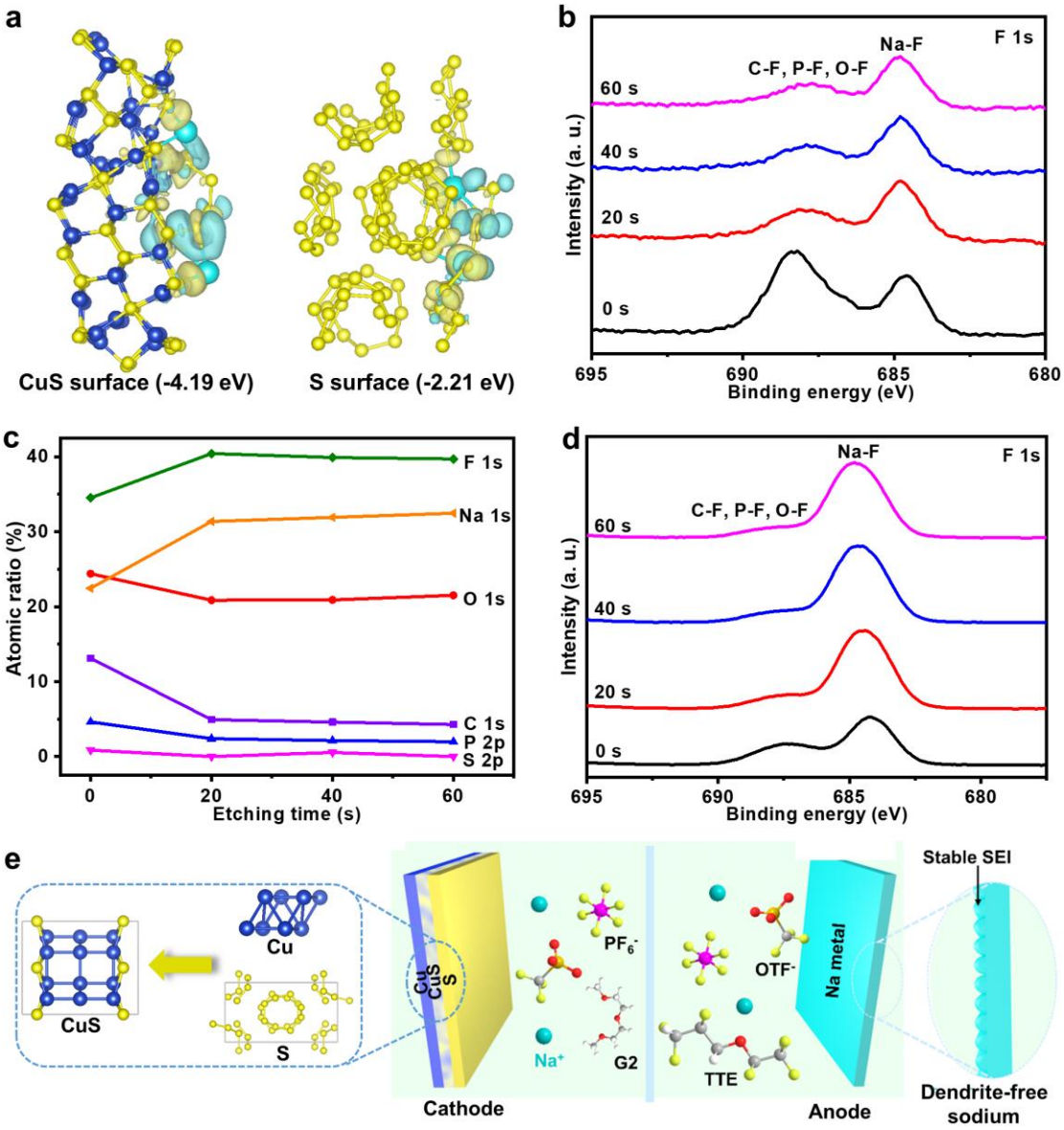

Figure 5. (a) Difference of charge density and the corresponding adsorption energy for the most stable configuration of CuS (left) and S (right) combined with the Na_2S_4 molecule, where the yellow and cyan regions are corresponded to electron accumulation and depletion, respectively. (isovalue=2×10^{-3} e $Bohr^{-3}$) Blue, yellow, and cyan balls represent Cu, S, and Na atoms, respectively. (b) The F 1s spectra at different etching time of the electrode harvested from sodium metal batteries after three cycles at 0.2 C. (c) The atomic ratios of C, O, P, F, Na and S in the SEI layer formed on Na metal anode at different etching time after three cycles at 0.2 C and (d) the corresponding F 1s spectra. (e) Schematic illustration of sodium metal batteries with the TTE-modified dual-salt electrolyte, Na metal anode, and micro-sized sulfur particles coated on the Cu current collector as the electrode.